Mira, Maria; Weiss, Marie; Baret, Frédéric; Courault, Dominique; Hagolle, Olivier; Gallego-Elvira, Belen; Olioso, Albert. 2015. **The MODIS (collection V006) BRDF/albedo product MCD43D: temporal course evaluated over agricultural landscape**. *Remote Sensing of Environment*, 170. 216-228. 10.1016/j.rse.2015.09.021

The MODIS (collection V006) BRDF/albedo product MCD43D: temporal course evaluated over agricultural landscape

Maria Mira[a,b,c*], Marie Weiss[a,b], Frédéric Baret[a,b], Dominique Courault[a,b], Olivier Hagolle[d], Belén Gallego-Elvira[e], Albert Olioso[a,b]

[a] *French National Institute for Agricultural Research (INRA), EMMAH – UMR 1114, 84914 Avignon, France*

[b] *University of Avignon and the Vaucluse (UAPV), EMMAH – UMR 1114, 84914 Avignon, France*

[c] *Grumets research group, Department of Geography, Universitat Autònoma de Barcelona (UAB), 08193 Bellaterra, Catalonia, Spain*

[d] *Center for the Study of the Biosphere from Space (CESBIO), EMR5126 (CNES-CNRS-UPS-IRD), 31401 Toulouse, France*

[e] *NERC Centre for Ecology and Hydrology, Wallingford, Oxfordshire OX10 8BB, United Kingdom*

[*] *Maria.Mira@uab.cat*

Abstract

The assessment of uncertainties in satellite-derived global surface albedo products is a critical aspect for studying the climate, ecosystem change, hydrology or the Earth's radiant energy budget. However, it is challenged by the spatial scaling errors between satellite and field measurements. This study aims at evaluating the forthcoming MODerate Resolution Imaging Spectroradiometer (MODIS) (Collection V006) Bidirectional Reflectance Distribution Function (BRDF)/albedo product MCD43D over a Mediterranean agricultural area. Here, we present the results from the accuracy assessment of the MODIS blue-sky albedo. The analysis is based on collocated comparisons with higher spatial resolution estimates from Formosat-2 that were first evaluated against local in situ measurements. The inter-sensor comparison is achieved by taking into account the effective point spread function (PSF) for MODIS albedo, modeled as Gaussian functions in the North-South and East-West directions.

The equivalent PSF is estimated by correlation analysis between MODIS albedo and Formosat-2 convolved albedo. Results show that it is 1.2 to 2.0 times larger in the East-West direction as compared to the North-South direction. We characterized the equivalent PSF by a full width at half maximum size of 1920 m in East-West, 1200 m in North-South. This provided a very good correlation between the products, showing absolute (relative) Root Mean Square Errors from 0.004 to 0.013 (2% to 7%), and almost no bias. By inspecting 1-km plots homogeneous in land cover type, we found poorer performances over rice and marshes (i.e., relative Root Mean Square Error of about 11% and 7%, and accuracy of 0.011 and -0.008, respectively), and higher accuracy over dry and irrigated pastures, as well as orchards (i.e., relative uncertainty <3.8% and accuracy <0.003). The study demonstrates that neglecting the MODIS PSF when comparing the Formosat-2 albedo against the MODIS one induces an additional uncertainty up to 0.02 (10%) in albedo. The consistency between fine and coarse spatial resolution albedo estimates indicates the ability of the daily MCD43D product to reproduce reasonably well the dynamics of albedo.

Keywords: albedo, MODIS, Formosat-2, validation, time series, observation coverage, point spread function, BRDF, narrow-to-broadband, surface reflectance, crop, regional scale.

1. Introduction

Land surface albedo is a critical variable affecting the Earth's climate, and accurate estimates are required to prevent uncertainties in the radiative budget of climate models (Brovkin et al. 2013). It is also essential for local and regional estimates of energy and mass exchanges between the Earth surface and the atmosphere, as described by soil-vegetation-atmosphere-transfer models (Bastiaanssen et al. (1998); Olioso et al. (1999); Tang et al. (2010); Merlin (2913)). Instantaneous albedo is a dimensionless characteristic of the soil-plant canopy system which represents the fraction of solar energy reflected by the surface. It is expressed as the ratio of the radiant energy scattered upward by a surface in all directions, compared to that received from all directions, integrated over the wavelengths of the solar spectrum (Pinty and Verstraete 1992). Albedo depends on the irradiance conditions and thus varies constantly throughout the day (Kimes et al. 1987). It can be represented by the weighted sum of the black-sky albedo (associated to the direct radiation coming from the Sun) and the white-sky albedo (associated to the diffuse radiation assumed as isotropic) (Schaepman-Strub et al. 2006). Uncertainties in albedo may induce significant uncertainties in the estimation of surface energy fluxes required to estimate evapotranspiration (i.e., net radiation, sensible heat flux, or soil heat flux). A simple calculation shows that an uncertainty of 0.02 in albedo (roughly equivalent to 10% error in albedo for agricultural landscape) induces a relative uncertainty on net radiation of around 5%. This was demonstrated by Jacob et al. (2002a) showing that, in the context of mapping evapotranspiration, an uncertainty of 10% in albedo may result in an absolute error of 20 $W \cdot m^{-2}$ in net radiation. The sensitivity analysis carried out by Bhattacharya et al. (2010) showed that an uncertainty of 10% for albedo induces uncertainties of about 2.0–5.9% on net radiation, of the order of 1.0–1.6% on the soil heat flux, and a strong influence on the evaporative fraction (i.e., ratio of latent heat flux to the sum of latent and sensible fluxes) showing a sensitivity of 2.7–21.4 %. As a result, the overall sensitivity of albedo on latent heat flux (which is directly related to evapotranspiration) was 7.0–21.4% (Bhattacharya et al. 2010).

Earth observation from satellite remote sensing provides synoptic and timely coverage which can be used to monitor albedo values from local to regional scales. The NASA's Earth Observing System program provides series of high-level land surface products including albedo at resolutions from 0.5 to 5 km derived from MODerate Resolution Imaging Spectroradiometer (MODIS) reflectances. These data are very useful for various operational applications since they are pre-processed, free and readily available to the scientific community. Nevertheless, to provide complete, physically consistent, global, and long-term land property data records, it is critical to understand and quantify the uncertainties associated to these products. Their validation still remains problematic because point-based measurements at the ground level are not suitable for direct comparisons with coarse or moderate spatial resolution satellite data over heterogeneous landscapes. Individual point-based measurements may not be representative of the surrounding area, unless the land cover, substrate, etc., in the region are reasonably homogeneous. In the past, these scaling differences have resulted in errors of the order of a 15% disagreement between the MODIS and field-measured values (Jin et al. (2003); Salomon et al. (2006); Liu et al. (2009); Roman et al. (2010); Wang et al. (2012); Wang et al. (2014)). To deal with such problems, local ground measurements are first used to validate high-resolution images of albedo estimates, which are then aggregated to evaluate collocated coarser resolution images (Liang et al. 2002; Susaki et al. 2007).

The high spatial and temporal resolution of Formosat-2 sensor (launched in 2004) provides a good opportunity to evaluate coarse resolution products over time. Formosat-

2 delivers daily 8 m spatial resolution data using a constant viewing angle thanks to an orbit with a 1-day repeat cycle. The good consistency between Formosat-2 and MODIS surface reflectances at the Climate Modeling Grid (CMG) spatial resolution (i.e., 0.05 degrees) was demonstrated by Claverie et al. (2013). They performed direct comparisons of surface reflectances derived from Formosat-2 and MODIS acquired on simultaneous days. After Bidirectional Reflectance Distribution Function (BRDF) correction, Formosat-2 reflectances were aggregated at CMG resolution by simple averaging. They found a very good agreement for all bands and with an accuracy higher than 0.01; however some degradation for the blue band due mainly to a high influence of aerosol content in this wavelength was observed.

The MODIS-BRDF/albedo standard product (i.e., MCD43), available globally since 2000, has been validated up to Stage 3 (for more details see (WWW1)) as defined by the Committee on Earth Observation Satellites (CEOS) (i.e., over a widely distributed set of locations and time period via several ground-truth and validation efforts) (Cescatti et al. 2012). According to the Global Climate Observing System, the accuracy requirement for albedo is about 5% (GCOS 2006), while the accuracy requirements established for the high-quality MODIS operational albedos at 500 m is, in general, 0.02 units or 10% of surface measured values maximum. As shown by validation results (Roman et al. (2009); Roman et al. (2010); Cescatti et al. (2012) ; Roman et al. (2013)) this level of accuracy is generally met, with discrepancies occurring during times of rapid change when the multiday algorithm can lag the actual changes in surface albedo. Recently, by improving the validation methodology, Roman et al. (2013) provided a 7.8% retrieval accuracy for the MODIS shortwave albedo by local (tower-based) and regional (airborne-based) assessment. Improvement came from the removal of measurement uncertainties when directly scaling up the tower albedo results to the

MODIS (500 m) satellite footprint, and from the reduction of uncertainties resulting from spatial aggregation of linear BRDF model parameters (Roman et al. 2011).

A continuing challenge in comparing albedo retrievals from different spatial resolutions is the necessity to ensure a good match between the observational footprints of both products. In fact, the observational footprint of a sensor is not the geometric projection of a rectangular pixel onto the Earth's surface (Cracknell 1998) due to the point spread function (PSF) of the system, which describes the response of the imaging system to a point source or point object. This induces some overlapping between contiguous pixels (Markham 1985). When considering across-track scanning sensors such as MODIS, the pixel overlap also depends on the view zenith angle (Gomez-Chova et al. 2011). Further, when considering processed data products instead of the actual physical quantity measured by the sensor (luminance), the footprint of the product is also affected by the different processing steps: geo-location uncertainty, spatial resampling, atmosphere scattering, viewing geometry, temporal synthesis (Weiss et al. 2007). Finally, scattering of light in the atmosphere contributes also to adjacency effects, enlarging the PSF differently for each waveband (Tanré et al. 1987). Therefore, an “equivalent PSF” that takes into account all of these features must be considered. This is particularly true when considering heterogeneous landscapes (Duveiller and Defourny 2010).

Up to now, the MODIS-BRDF/albedo is derived by inverting a BRDF model over multi-date, multi-angular, cloud-free, atmospherically corrected, surface reflectance observations acquired by MODIS instruments on board the Terra and Aqua satellites during a 16-day period. A disadvantage of such a composite product comes from its poor ability to capture albedo trends under conditions of seasonal or rapid surface change. A daily composite product will be released in the near future: the MCD43 Collection V006 albedo product. The objective of this study is to evaluate the uncertainty of MCD43D product (30 arcsec CMG, daily, 16-days retrieval period) over a Mediterranean agricultural region as well as its consistency over time. High spatial and temporal resolution Formosat-2 data (8 m, daily), previously evaluated with ground measurements concurrently acquired over the same study area, are used as a reference. The footprint issue is accounted for by computing the MODIS "equivalent PSF".

2. Materials

The same dataset used by Bsaibes et al. (2009) was used in this study: ground albedo measurements and Formosat-2 images both acquired over the Crau-Camargue site during 2006. Additionally, we used MODIS images and ancillary data necessary to compute the blue-sky albedo.

2.1. The Crau-Camargue site

The Crau-Camargue study area is located in the lower Rhône Valley, South Eastern France (50 km around 43.56°N; 4.86°E; 0 to 60 m above sea level). It is mainly a flat area which presents a wide variety of land covers including dry and irrigated grasslands, wetlands and various crops (see Fig. 1). The experiment took place in 2006, including intensive ground measurements simultaneously collected with satellite data on various crop types (Courault et al. 2008). Low cumulative precipitation was observed in 2006 (456 mm) as compared to the average (548 mm between 2001 and 2010). The weather was especially dry from April 1st to mid-September 2006, with three sparse rainfall events (less than 30 mm/day).

[Insert Fig. 1 about here]

The most dominant land cover, at the center of the site, corresponds to a large and flat stony area of more than 74 km^2. It is covered by a specific dry grass ecosystem (locally termed 'coussoul'). In spring and autumn, the 'grass' is grazed by sheep; in summer, the vegetation dries out quickly; in winter, the vegetation is dry. Around the 'coussoul', there are a wide variety of land covers including irrigated grasslands and crops (wheat, maize, corn, sorghum, rice and orchards). They are generally arranged in small plots of less than 0.5 km^2, with a large range of sizes and shapes (Fig. 1). The South West of the area, located in the Camargue within the Rhône delta, is dominated by wetlands, salty marshes (locally known as 'sansouires') and paddy rice crops. Depending on the availability of water originating from rice irrigation and shallow water tables, ecosystems of Camargue can be either very dry or very humid. Two small ponds are located at the North and others at the South East around the biggest one (Berre pond), of which only a small portion is within the study region. Apart from few roads, two villages are located next to the Berre pond.

The land cover was classified following a maximum likelihood supervised classification, using the four Formosat-2 spectral bands and five images distributed throughout the experimental period, selected by considering the temporal dynamics of vegetation cover. Eight classes were identified, which included the main vegetation covers, free water and urban areas. In this study, this map is only used to illustrate the homogeneity of the land cover type at 1-km scale and the associated uncertainty will therefore not affect the results of this study.

2.2. Main features of the sampled fields

Five fields were equipped with pyranometers to monitor albedo throughout the growing season (Fig. 1). They were mainly selected to represent different vegetation types and conditions that determine the range of albedo values. The two wheat fields (#1 and #2) were sown on November 11th and December 15th, and harvested on June 27th and July 4th, respectively. They were not irrigated, and turned to bare soils or were covered by stubble after harvest (stubble may have very large albedo, Davin et al. (2014)). The meadow field (#3) was flooded every 11 days. Three cuts were performed during the growing season, on May 5th, July 7th, and August 11th. The maize field (#4) was sown on May 5th, and intermittently irrigated by sprinklers depending on weather conditions. It was finally harvested on August 8th. The rice field (#5) was sown on dry soil on April 27th, then continuously submerged from May 5th till October 6th with a 0.10±0.05 m water height, and finally harvested on October 18th. Due to strong winds, the field was subjected to stem lodging after August 30th.

2.3. Ground albedo measurements

Albedo was measured at the five fields with Kipp & Zonen (Delft, The Netherlands) conventional pyranometers (type CM7), which measure radiation in the 300–3000 nm spectral range. The sensors, one facing up and one facing down, were mounted between 1.5 m and 2 m above top of canopy. Measurements were made every 15 seconds and averaged over 10 minute periods throughout vegetation cycles. The measurement footprints were circular, with 80% of the signal coming from a region of diameter between 6 to 8 m. The sensors were calibrated against reference radiation sensors, following (ISO 1992) and (WMO 2008) leading to an uncertainty of about 6%.

2.4. Formosat-2 images

Formosat-2 is a Taiwanese satellite launched by the National Space Organization in May 2004 into a sun-synchronous orbit (Chern and Wu 2003). It is a high-resolution optical sensor characterized by a daily revisit frequency and constant viewing geometry. With its 24-km swath, it collects images with an 8 m nadir spatial resolution, in four wavebands of 90 nm width centered at 488, 555, 650 and 830 nm. The Crau–Camargue site was observed with rather constant viewing zenith (41°) and azimuth (239°) angles.

Images were recorded every three to six days at 10:30 UTC from March to October 2006. They were ortho-rectified following Baillarin et al. (2004), radiometrically calibrated and corrected for atmospheric effects following Hagolle et al. (2015). The final output product provides surface reflectance images with cloud and cloud shadow masks from Hagolle et al. (2015). Water bodies and snow surfaces were identified as well. The absolute location accuracy is better than 0.4 pixel, i.e. 3.2 m (Baillarin et al. 2008). Over the 36 images collected between March and October, 31 images were cloudless, with some gaps (less than 2 weeks) due to the presence of clouds: from March 12th to April 2nd, April 14th to May 14th, and after August 22nd.

2.5. Albedo estimates from Formosat-2 images

Bsaibes et al. (2009) proposed a simple empirical transfer function. It was calibrated over all the available dates and crops (wheat, maize, rice and meadow), representing a total of 130 ground based blue-sky albedo and corresponding Formosat-2 data:

$$\alpha_{FORMOSAT-2} = 0.619 * \rho_{Red} + 0.402 * \rho_{NIR} \tag{1}$$

where ρ are the Formosat-2 reflectances in band 3 (Red) and band 4 (NIR). The pyranometer measurements were associated to Formosat-2 data aggregated over a 32×32 m^2 area (4×4 pixels). It should be noticed here that Eq. (1) relates the blue-sky albedo that depends on the atmosphere diffuse fraction, to atmospherically corrected reflectance. However, the top of canopy – reflectance – blue-sky albedo relationship was calibrated by Bsaibes et al. (2009) using 30 different dates providing very good performances ($RMSE_R$ of 7.5% and negligible bias). This indicates that, for this study the impact of diffuse fraction, and thus atmospheric conditions, is low. These evaluation results were comparable to calibration residual errors reported by Liang et al. (1999), Weiss et al. (1999) and Jacob et al. (2002b), and were close to relative accuracy of albedo measurements with the pyranometers and Formosat-2 corrected data (around 5%). Far from providing a generic and robust mean of estimating albedo using Formosat-2 data, the limitation of estimating albedo following Eq. (1) lies in their application to our study region and retrieval period. To extrapolate the results to other areas and time periods, local calibration would be needed.

2.6. MODIS and ancillary data used to compute blue-sky albedo

The reprocessed (V006) merged Terra and Aqua MODIS BRDF/albedo product MCD43D, is produced in a 30 arcsec resolution CMG in a global geographic lat-long projection (see Table 1). This product will be soon released through LAADS (WWW2) and was kindly provided by Prof. Crystal Schaaf (University of Massachusetts, Boston) and her team. Conversely to the previous version (i.e., MCD43B 1 km tiled products), the V006 collection is retrieved daily (versus the 8-day synthesis period for V005) and separately from the 500 m BRDF/albedo model parameters product MCD43A1: all the observations from both the Terra and Aqua satellites within a 30 arcsec grid (i.e., only the 500 m and 250 m MODIS channels are used, and not any of the 1 km MODIS channels) and comprised within a 16-day moving window are used to retrieve the BRDF model parameters, while the previous version averaged the underlying 500 m product, leading to a lower quality. During the compositing period, daily data are weighted as a function of the quality, the observation coverage and the temporal distance from the day of interest. The date associated to each daily V006 retrieval is the center of the moving 16 day window while the date attributed to the V005 product was the first day of the 16 day window. More details about the V005 MCD43B albedo product can be found in Roman et al. (2013) and Schaaf et al. (2010). The MCD43 product is estimated via inversion of reciprocal version of the RossThick-LiSparse kernel-driven semiempirical

BRDF model (Ross (1981); Li and Strahler (1992); Schaaf et al. (2011)). The MCD43D product includes the BRDF/albedo model parameters (i.e., isotropic, volumetric and geometric kernels weights) for each MODIS spectral band and for three broad bands (visible, near infrared and shortwave), used to compute albedo for any solar illumination geometry.

[Insert Table 1 about here]

In this study, the directional hemispherical reflectance (black-sky albedo) and the bi-hemispherical reflectance for isotropic diffuse illumination conditions (white-sky albedo) were computed for the shortwave band (0.3-5.0 μm). For that, we considered the three BRDF/albedo model parameters for the shortwave (on products MCD43D28, MCD43D29 and MCD43D30, one in each), the solar illumination geometry corresponding to Formosat-2 acquisition time (10:30 UTC), and the coefficients found by Lucht et al. (2000a) and Lucht et al. (200b) to estimate black-sky and white-sky albedos following the kernel BRDF model. Data were filtered to highest quality for all the bands (i.e., 'snow-free albedo retrieved' and 'good quality' from the *BRDF_albedo_quality* and the *BRDF_albedo_band_quality* products).

3. Methods

3.1. Blue-sky albedo estimates from MODIS images

The albedo (α) for the shortwave band under actual atmospheric conditions (hereafter blue-sky albedo, but also referred as actual or real albedo in the literature) is modeled quite accurately as a sum of the black-sky (α_{BS}) and white-sky albedos (α_{WS}) weighted by the fraction of diffuse skylight (S):

$$\alpha(\theta) = \left(1 - S(\theta, \tau_{550nm})\right) * \alpha_{BS}(\theta) + S(\theta, \tau_{550nm}) * \alpha_{WS}(\theta) \qquad (2)$$

where θ is the solar zenith angle, and τ_{550nm} is the atmospheric optical depth at 550 nm used to derive the fraction of diffuse skylight for the shortwave (Lewis and Barnsley 1994; Lucht et al. 2000b). For our study region, we used a 6S radiative transfer code (Vermote et al. 1997) precomputed look-up table freely released by the MODIS community at (WWW3) which allows estimating S using θ, τ_{550nm} and the aerosol type as inputs. We considered the shortwave MODIS broad band, the continental aerosol model type and the solar zenith angle θ at 10:30 UTC over each 30 arcsec pixel (ranging from 24.7° to 51.1°). The optical depth τ at 550 nm estimated by Hagolle et al. (2015) for atmospheric correction of Formosat-2 images was compared with that retrieved from the following 3 sources, depending on their availability following this order (Fig. 2):

- For 14 dates, Aerosol Robotic Network (AERONET; Holben et al. (1998)) observations from 'La Crau' station located at the center of the study area and at about 15 km East of pyranometers location (see Fig. 1).
- For 8 dates, AERONET observations from the 'Avignon' station located at about 33 km North of pyranometers location.
- For the remaining 9 dates, MODIS Aerosol data product MOD04_L2 closest in time to 10:30 UTC (no data were available on product MYD04_L2). We considered only the best quality data by selecting a QA confidence flag of 3. According to Remer et al. (2006), the associated accuracy of this product is 0.05. Since aerosol optical properties vary slowly with location (Hagolle et al. 2015), these daily Level 2 data are produced at the spatial resolution of a 10×10 1-km (at nadir)-pixel array. We then spatially interpolated the MODIS aerosol product at the center of the study area.

[Insert Fig. 2 about here]

We observed τ_{550nm} bias of about 0.015 (and absolute Root Mean Square Error of 0.03) from MOD04_L2 product compared to data from AERONET La Crau measurements (14 dates). This leads to an overestimation of about 0.10 for the fraction of diffuse skylight, and a negligible error in the blue-sky albedo (i.e., <0.0003). A sensitivity analysis (not shown here for the sake of brevity) demonstrated that, for our study area and period, only errors in τ_{550nm} higher than 0.05 induce errors higher than 0.001 on the blue-sky albedo. Therefore, the diffuse fraction estimated with MOD14_L2 aerosol product could be considered as a good approximation for our study. Nevertheless, to keep temporal consistency throughout the year and because the comparison with AERONET data provides good results (bias of 0.03 and absolute Root Mean Square Error of 0.047), we decided to consider the optical depth estimates from Hagolle et al. (2008), consistent with the atmospheric correction performed on the Formosat-2 images. The τ_{550nm} values were ranging from 0.013 to 0.323, corresponding to a 0.08 to 0.24 fraction of diffuse skylight (Fig. 2).

MODIS images were re-projected from their initial projection (Sinusoidal) to the Formosat-2 data projection (France Lambert II étendu, nouvelle triangulation Française IGN) using the MODIS reprojection tool (WWW4). Further, spatial resolution was set to exactly 1000 m instead of 30 arcsec CMG by considering bilinear resampling for albedo data and nearest neighbor resampling method for quality control data.

3.2. Estimating the equivalent MODIS PSF from albedo product

A methodology based on image correlation analysis was developed to assess the equivalent PSF for MODIS albedo products over the Crau-Camargue area to perform spatially consistent evaluation of the MCD43D product using Formosat-2 data. Given the large difference in spatial resolution between Formosat-2 and MODIS, the Formosat-2 PSF was approximated by the pixel area itself.

3.2.1. MODIS PSF model

The product PSF results from a number of processes that need to be accounted for. The instrument PSF depends on several components: the electronic PSF, the detector PSF, the image motion PSF, and the optical PSF (Schowengerdt 2007). According to Duveiller et al. (2011), electronic and image motion PSFs can be neglected. Then, the PSF for the MODIS instrument can be approximated by the convolution of a Gaussian function characterizing the optical PSF with the detector PSF modeled as a triangular PSF in the cross-track direction and as a rectangular PSF in the along-track direction. However, at the product level, the temporal compositing and spatial resampling also contribute significantly to the PSF. Considering these multiple contributions, we propose to describe the equivalent PSF by a Gaussian function. However, because of the deformation of the footprint for the across track observations due to the intrinsic detector characteristics, we propose to use an asymmetric Gaussian function. At a first sight, given the Terra and Aqua inclination angle of around 98°, the rotation axis of the PSF should be oriented along-track. However, a significant part of the PSF comes from the projection that requires interpolations carried out according to two directions (Latitude and Longitude). Therefore, given the low angular deviation of the platforms from the North (8°), we considered an asymmetric Gaussian function between the North-South direction and the East-West direction (Fig. 3):

$$PSF(x,y) = \frac{G(x,y)}{\int_{x=0}^{xmax} \int_{y=0}^{ymax} G(x,y)\cdot dx \cdot dy} \tag{3a}$$

$$G(x,y) = \frac{e^{-(a(x)+a(y))}}{(\sigma_x \sigma_y)^2 \sqrt{2\pi}} \tag{3b}$$

$$a(x) = \frac{\boldsymbol{x}^2}{2{\sigma_x}^2} \quad ; \quad a(y) = \frac{\boldsymbol{y}^2}{2{\sigma_y}^2} \tag{3c}$$

where $\boldsymbol{x}$ and $\boldsymbol{y}$ are the distances to the center of the PSF in the East-West and North-South dimensions, and σ_x and σ_y the standard deviations of the distances in East-West and North-South dimensions, respectively. The PSF is characterized by the Full Width at Half Maximum (*FWHM*) of the two Gaussian functions:

$$FWHM_x = 2\sqrt{2ln(2)}\sigma_x \quad ; \quad FWHM_y = 2\sqrt{2ln(2)}\sigma_y \tag{4}$$

Contrary to the Gaussian function, the PSF is not infinite. We therefore conducted a sensitivity analysis to define the minimum PSF value at which the Gaussian distribution should be truncated, hereafter called the *'PSF_{min}'*.

[Insert Figure 3 about here]

3.2.2. Estimating the equivalent PSF of MODIS albedo using Formosat-2 data

To reduce the computational time for the PSF assessment and correct possible change in spatial resolution of Formosat-2 data for being targeted off-nadir, Formosat-2 albedo pixels were aggregated by 5×5 pixels to provide a 40 m resolution cell. Besides, since the method requires no missing data, images were cropped (remaining of about 15×30 km^2, plotted in Fig. 1), and a specific processing over cloud and cloud shadow pixels was applied. Similarly to the strategy followed to produce the MODIS albedo, based on a 16-day compositing, we assumed that albedo was almost steady during a short period of few days. The albedo value of cloud and cloud shadow pixels was set to the Formosat-2 albedo value of the same pixels at the closest clear date (e.g., usually 3 to 6 days difference, and exceptionally 12 days for acquisitions on day of year 234 and 246).

The MODIS albedo equivalent PSF was retrieved by maximizing the correlation coefficient between the moderate resolution (*MR*) image (i.e., MODIS blue-sky albedo) and the corresponding higher resolution (*HR*) image (i.e., Formosat-2 albedo) convolved with the PSF Gaussian Model (HR_{agg}):

$$HR_{agg}(x_o, y_o) = HR(x, y) \otimes PSF(x, y) \tag{5}$$

where each pixel of the resulting image HR_{agg} corresponded to a MR observation centered at (x_0,y_0) and $\otimes$ is the convolution symbol. The correlation coefficient (C) between HR_{agg} and MR was then computed as:

$$C = \frac{\sum_{i=1}^{N}\left(HR_{agg\,i} - \overline{HR_{agg}}\right)(MR_i - \overline{MR})}{\sqrt{\sum_{i=1}^{N}\left(HR_{agg\,i} - \overline{HR_{agg}}\right)^2 \sum_{i=1}^{n}(MR_i - \overline{MR})^2}} \tag{6}$$

where subscript i refers to each pixel at the moderate resolution, $\overline{MR}$ (respectively $\overline{HR_{agg}}$) to the MR (respectively HR_{agg}) image mean value, and N to the number of valid moderate resolution pixels used for the comparison. The PSF was estimated by considering a range of $FWHM_x$ (i.e., from 1400 to 2360 m) and $FWHM_y$ (i.e., from 800 to 1840) by steps of 40 m. To make the results comparable, we considered the same area extent throughout this study.

During the optimization process of the PSF parameters, we considered possible geolocation errors between each Formosat-2 and MODIS image, characterized by a shift in x and/or y location between both images. We used an iterative approach which consisted in using the smallest PSF (i.e., $FWHM_x$=1400 m, $FWHM_y$=800 m) to determine a first guess of the x/y shift that provided the highest correlation between the MODIS and Formosat-2 image. Then, the mis-registration was refined by shifting the HR image 1000 m up and down in both x and y directions by steps of 40 m and computing the resulting C value for all possible PSF sizes. This resulted in a set of 1,687,500 combinations for each day. Daily optimal PSF sizes were computed, as well as an optimal PSF size by considering all dates together. In both cases, mis-registration effects from each image were corrected separately.

3.3. MODIS albedo evaluation

Because urban and water land covers were neither used for the calibration of the regression Eq. (2), nor for its evaluation, we excluded MODIS pixels containing more than 50% of cloud, cloud shadows, urban or water areas (e.g., of about 9% of 1-km pixels, mostly located on the Eastern part of the image). The MODIS product quality flag was also used to keep only MODIS albedo data of best quality. To further analyze the impact of land cover on the evaluation results, a set of pixels characterized by a predominant land cover type were selected. The composition of these pixels in terms of land cover type was computed without considering boundary pixels within the PSF footprint: the variation of the PSF size between days would imply too much complexity for this analysis. Nevertheless, the weights associated to these pixels are very low and correspond to the tail of the Gaussian function.

Three metrics were considered to quantify the deviation between both datasets: the bias, the absolute ($RMSE_A$) and the relative ($RMSE_R$) Root Mean Square Errors, used to quantify the accuracy, the absolute uncertainty and the relative uncertainty, respectively (Vermote and Kotchenova 2008):

$$Bias = \frac{1}{N}\sum_{i=1}^{N}(HR_{agg\,i} - MR_i) \quad (7)$$

$$RMSE_A = \sqrt{\frac{1}{N}\sum_{i=1}^{N}\left(HR_{agg\,i} - MR_i\right)^2} \quad (8)$$

$$RMSE_R = \frac{RMSE_A}{HR_{agg}}100 \quad (9)$$

4. Results and discussion

4.1. MODIS albedo product PSF

Fig. 4 and Fig. 5 provide results to illustrate the assessment of the PSF of the MODIS albedo product using Formosat-2 data by differentiating mis-registration correction effects (Fig. 4a and Fig. 5a) and PSF size effects (Fig. 4b and Fig. 5b): in the first case, we used the PSF size that provided the highest correlation *C* for each shift; in the second case, we used the *x*/*y* shifts that provided the highest correlation for each PSF size in terms of $FWHM_x$ and $FWHM_y$. These results are shown for the 23rd July, 2006 (Fig. 4) and were similar for the other dates.

[Insert Fig. 4 about here]

[Insert Fig. 5 about here]

The maximum *C* is well identified (Fig. 4) even if the maximum of the 'curve' was relatively flat in the range of hundreds of meters. Such behaviors were observed every day, as indicated by the length of boxplots (Fig. 5). Considering the mis-registration correction (Fig. 5a), *C* varied within ±0.001 in the range of up to 200 m in both directions, and in average by 100 m. Considering the assessment of the PSF size (Fig. 5b), *C* varied within ±0.001 in the range of up to 480 m in *x* and 640 m in *y*, and in average 280 m and 360 m, respectively. This may be related to the degree of heterogeneity of the area in terms of albedo, and gives an idea about the minimum distance between surfaces highly contrasted in albedo.

The variability observed throughout the period for the optimum shift (i.e., 320 m in *x* and 440 m in *y*, for *C*±0.001) was related to the mis-registration of MODIS images, which can vary between days. According to Wolfe et al. (2002) the MODIS geolocation accuracy of the sensed 1 km observations at nadir is of 18±38 m in-track and 4±40 m cross-track. Nonetheless, these values cannot be taken as a reference for this study, because we consider a Level 3 product. The variability may also be related to the albedo spatial distribution as demonstrated by the variability of the optimum PSF size observed throughout the time period (i.e., 960 m in x and 760 m in y, for C±0.001), as well as to the distribution of angular measurements within the time window used for the BDRF calibration (which necessarily encompass different footprints). Nevertheless, the MODIS albedo PSF was always larger in one direction (x axis) than in the other (y axis). In average, it was larger by a factor of 1.6, ranging from 1.2 to 2.0. Commonly, the PSF was characterized by $FWHM_x$=1920 m and $FWHM_y$=1200 m, with values ranging from 1400 to 2360 m and from 1040 to 1360 m. This is in agreement with Tan et al. (2006), who showed that the linear dimension of the area sensed in the along-scan direction is twice as long as the nominal observation size, due to the triangular shape of the MODIS PSF in that direction. Conversely, in the along-track direction, the PSF is still approximately rectangular (Nishihama et al. (1997); Barnes et al. (1998)). This effect, so called as the "bow tie" effect, was mentioned by Wolfe et al. (1998) who stated that the projection of a MODIS detector's instantaneous field of view onto the surface is approximately 2.0 and 4.8 times larger at the scan edge than at nadir in the track and scan directions, respectively.

4.2. Impact of the PSF on the product value

Fig. 6 presents the blue-sky albedo estimated over the area by Formosat-2 at 40 m (Fig. 6a), Formosat-2 at 1 km obtained by simple averaging (Fig. 6b), Formosat-2 at 1 km by considering the PSF (Fig. 6c), and MODIS at 1 km (Fig. 6d) for the 23rd of July (2006).

[Insert Fig. 6 about here]

These figures show that the albedo spatial distribution is similar between the two spatial resolutions (i.e., 1000 m and 40 m): the highest albedo values (up to 0.25) are observed at the center of the image and correspond to the dry grass over ‘coussoul’; on the left, the lowest albedo values (of about 0.05) are obtained over the swamps; while crops depict medium albedo values such as observed in the orchard fields located inside ‘coussoul’. High albedo values are observed over small agricultural fields at 40 m spatial resolution, likely because of the presence of stubble (Davin et al. 2014). Albedo ranged from 0.11 to 0.22, the majority ranging from 0.15 to 0.19, although the decrease in spatial resolution implies a decrease in the albedo. The effect of not considering the actual pixel footprint, but the geometric projection of a rectangular area onto the Earth’s surface implies more contrast in albedo between contiguous pixels (Fig. 6b). The PSF generally brightens dark objects and darkens bright objects, which induces a smaller range of values. This was in agreement with experimental results from Huang et al. (2002), who analyzed the impact of sensor PSF on land cover characterization using MODIS reflectances at 250 m.

Fig. 7 presents a density scatter plot between MODIS blue-sky albedo from the 31 dates over the same area and Formosat-2 albedo convolved with the PSF (Fig. 7a) or aggregated using a simple average over a squared 1 km^2 area (Fig. 7b). Note here that the mis-registration was corrected for each date.

[Insert Fig. 7 about here]

There is a very good agreement between MODIS blue-sky and PSF aggregated Formosat-2 albedos, with a very good uncertainty of 0.007 in absolute and 4% in relative (Fig. 7a). When applying a simple averaging, we observe a higher scattering than when using PSF convolution: the uncertainty is doubled while the accuracy remains quite the same (Fig. 7b). When analyzing statistics from each considered date, we observed that neglecting the PSF of MODIS albedo induced an additional uncertainty up to 0.02 (10%)."

Once we assessed the $FWHM_x$ and $FWHM_y$ for each date, we performed a sensitivity analysis to PSF_{min}, i.e. the value used to cut the Gaussian function that models the PSF. We found no difference between the resulting Formosat-2 and MODIS albedo products (i.e., bias, $RMSE_A$ and $RMSE_R$ are about the same) using PSF_{min} values varying between 0.20 and 0.015. For reference, a PSF_{min} value of 0.015 was used by Weiss et al. (2009) with the same methodology to determine the PSF of MERIS FAPAR (i.e., fraction of photosynthetically active radiation absorbed by the canopy). Mis-registration effects were corrected for each date. Note here that the smaller the PSF_{min}, the higher the PSF and the smaller the possible extent of the study area. Even though, if the optimum PSF size is characterized for each PSF_{min}, the convolved albedo products are about the same even for PSF_{min}=0.5, demonstrating that the change in PSF size is able to compensate for PSF_{min} effects, without this downplaying the importance of considering the PSF. The slight impact of PSF_{min} may be related to the high spatial homogeneity in albedo and the small extent of the area selected for the study.

From the comparison between the optimal PSF size (i.e., $FWHM_x$=1920 m; $FWHM_y$=1200 m) for our study site by considering all the dates together and the daily optimal PSF size (not shown here for the sake of brevity), we observed that C significantly decreases for the last acquisitions (i.e., down to 0.011 in the worst case). Indeed, the optimal common PSF $FWHM_x$ is much higher than the optimal daily $FWHM_x$ from late August (Fig. 5b). However, regardless of C values, the statistical metrics remain the same. Consequently, we can conclude that a good characterization of the equivalent PSF of MCD43D albedo product for acquisitions over our Mediterranean agricultural area, independently of the period of the year, was given by a PSF model characterized with $FWHM_x$=1920 m, $FWHM_y$=1200 m and any value for the PSF_{min} lower than 0.2.

4.3. Blue sky albedo

The effect of the fraction of diffuse skylight (*S*) was analyzed by comparing MODIS blue-sky albedo with Formosat-2 albedo (considered as blue-sky albedo also) convolved with the optimum PSF, each time from a set of days with certain range of values for *S* (Fig. 8).

[Insert Fig. 8 about here]

Relative uncertainties (i.e., 3 – 4 %) are of about the same order independently of the *S* level, and accuracies (i.e., <0.002) are acceptable for all cases. Nevertheless, we observe a MODIS albedo overestimation for small values of *S* (i.e., negative bias), and an underestimation (i.e., positive bias) for high values of *S*. This could be due to a slight overestimation of MODIS black-sky albedo product and a slight underestimation of MODIS white-sky albedo products, besides to the uncertainty in *S*.

4.4. MODIS albedo product evaluation against Formosat-2 blue-sky albedo

Along the 31 dates, the accuracy varied from -0.005 to 0.011, and the uncertainty (relative uncertainty) from 0.004 to 0.013 (2% to 7%) (Fig. 9), which are quite acceptable errors according to the 5% accuracy requirement stated by GCOS (2006). Results appear independent from the season. Note here that, only when the threshold value used to mask MODIS pixels containing cloud, cloud shadows, urban or water areas was reduced to 20%, statistics worsened significantly (i.e., an increase of bias and $RMSE_A$ equal or higher than 0.0010). Although the temporal variation of the fraction of diffuse skylight *S* is not clearly correlated to the albedo course (see Fig. 2), generally the higher the *S*, the lower the accuracy (see also Fig. 8c), while the uncertainty does not seem to be affected.

[Insert Fig. 9 about here]

Fig. 6d shows the selected set of pixels characterized by a predominant land cover type, while their composition is specified in Table 2. The evaluation performances and statistics of the comparison between MODIS and Formosat-2 albedo over each pixel are summarized in Table 2 and Fig. 10a. Fig. 11 presents the albedo temporal variation of the 5 land cover types together with the occurrence of rainfall events. For comparison, we include the correlation between MODIS and Formosat-2 albedos aggregated by simple average (Fig. 10b), showing again the importance of considering the PSF.

[Insert Fig. 10 about here]

[Insert Fig. 11 about here]

[Insert Table 2 about here]

The worst performances were observed over rice and marshes, with a relative uncertainty of 11% and 7%, respectively, and rather large accuracy (i.e., 0.011 and -0.008, respectively). Fig. 10a shows that, for albedos lower than 0.14, Formosat-2 provides higher albedo values over rice plots as compared to MODIS. As it is shown in Fig. 11, the agreement was good when the rice was in the vegetative or reproductive phase (i.e., from June to October), but worsened when it was sown on dry soil (i.e., from March to May) or submerged in water (i.e., from May to June). In contrast, there was a general underestimation of Formosat-2 albedo over marshes of about 0.008 (Table 2). These discrepancies are in agreement with the results found by Bsaibes et al. (2009) over rice and freshly cut meadows. This could be explained by the lack of shortwave infrared wavebands sensitive to water in the Formosat-2 configuration, besides the poor estimate of urban albedo by Formosat-2 in the case of the rice spot which contains about 9% or urban area. The other land cover types (i.e., dry pastures, irrigated pastures, and orchards) showed fairly low uncertainty (i.e., from 3.0% to 3.8%) and reasonably good accuracy (i.e., <0.003) (Table 2). Exceptionally, an unexplained behavior was observed for day of year 246 over dry pastures, not due to the presence of irrigated areas in the pixel extended to the PSF. Eq. (1) could be calibrated over each cover type to reduce the biases observed in Fig. 10. Nevertheless, the performances of applying a unique set of coefficients are here sufficient to further assess the energy balance (Mira et al. 2015). The main advantage is that no land cover map is required to run the algorithm.

The different patterns of the albedo dynamics captured throughout the study period by MODIS and Formosat-2 (Fig. 11) show a limited variability of the albedo partly caused by the fact that the images were acquired under clear sky conditions with a low diffuse component of solar irradiance. However, the albedo variability was larger over rice and dry pastures, which might mainly be due to the changes in surface properties characteristic associated to plant phenology and agricultural practices. The dynamics of the daily MCD43D albedo product are in good agreement with the one depicted by Formosat-2 albedo convolved with the PSF. Nevertheless, the variability exhibited by Formosat-2 is a little larger as observed from the comparison of data during the period with many acquisitions close in time (i.e., data from day of year 134 to 222). Similarly, Shuai et al. (2014) demonstrated that Landsat albedo exhibits more detailed landscape texture and a wider dynamic range of albedo values than the coincident 500-m MODIS operational products (MCD43A3), especially in heterogeneous regions. As stated by Ju et al. (2010), the BRDF model parameters may not serve as reliable *a priori* estimates of the surface anisotropy and may not capture the temporal dynamics of certain surface disturbances, such as fire or rapid snow melt. Gap filling methods are considered to overcome these limitations (for further details see Ju et al. (2010)). Locally, however, especially in periods of rapid phenological change and where there were remaining outliers, the reliability of albedo estimates could be reduced (Ju et al. 2010).

5. Conclusions

In this study, the forthcoming MODIS official albedo product MCD43D V006 (30 arcsec CMG, daily, 16-days retrieval period) was evaluated over a Mediterranean agricultural area. The evaluation was based on the comparison with estimates from high spatial and temporal resolution albedo (Formosat-2, 40 m, daily) acquired from March to October 2006, which were first evaluated at a local scale against field measurements by Bsaibes et al. (2009) and then aggregated to the coarse spatial resolution by considering the observational MODIS footprint.

At a local scale, the Formosat-2 albedo, estimated following the Narrow-To-Broadband conversion method by considering the red and near infrared bands, demonstrated a high level of robustness over the study area. It resulted in uncertainties of 0.015 when compared with in situ measurements acquired over five crop types.

This study provides a methodology to characterize the equivalent point spread function of MODIS albedo at 1 km. It is modeled as the product of two Gaussian functions, 1.2 to 2.0 times larger in East-West than North-South direction. The optimum PSF was characterized by $FWHM_x$=1920 m and $FWHM_y$=1200 m for all the dates, with values ranging from 1400 to 2360 m and from 1040 to 1360 m, respectively, when estimated daily. The analysis also demonstrates that evaluation results do not depend on the minimum PSF value at which the Gaussian distribution is truncated. This is partly due to the moderate heterogeneity level of the experimental area, and to a lesser extent to the compensation provided by the change in the $FWHM_x$ and $FWHM_y$ size. Conversely, mis-registration effects between the two sensors cannot be neglected and varied up to 320 m in East-West and 440 m North-South directions depending on the date. Finally, the convolution with a Gaussian PSF improved the MODIS albedo evaluation performance as compared to a simple averaging aggregation. These results demonstrate that the PSF must be considered to adequately evaluate MODIS 1-km albedo when using higher spatial resolution images, even if the heterogeneity in albedo does not appear very large.

Inter-comparison of MODIS and PSF-convolved Formosat-2 albedos highlighted the ability of the MCD43D V006 albedo product to estimate with high accuracy and low uncertainty the albedos from an agricultural region covering a variety of land covers, including dry and irrigated grasslands, wetlands and various crop types (wheat, maize, corn, sorghum, rice and orchards) during whole vegetation cycles. With 6662 pixels used for the comparison, MCD43D yielded an albedo uncertainty of 0.007 (4.0%), with no bias. Albedo estimates from dry pastures, irrigated pastures or orchards were accurate (<0.003), with low uncertainty (<0.006; <3.8%). On the contrary, albedo estimates from rice and marshes were less accurate (<0.011) and with a higher uncertainty (<0.015; <10.7%). These discrepancies were attributed to the lack of water sensitive shortwave infrared spectral bands within the Formosat-2 configuration. The inter-comparison displayed as well a good overall temporal consistency. The variability exhibited by Formosat-2 data was a little larger.

The method used in this study is sensitive to the heterogeneity of the area, with the constraint that a correct characterization of the PSF would not be possible on a homogeneous area. Nevertheless, for homogeneous areas, a simple averaging is sufficient to accurately evaluate the albedo. The method considers the optimization of the PSF to correlate the best Formosat-2 and MODIS images, which induces an intrinsic improvement of the evaluation results. However, this improvement was observed not only globally over the images as expected, but also over each individual pixel.

Nevertheless, these results are limited to a single experimental site over a range of diffuse fraction between 0 and 0.25. Therefore, to extrapolate the results from this study to other areas it is necessary to evaluate the methodology over independent experimental sites characterized by different types of vegetation, heterogeneity levels, and a larger range of atmospheric conditions. The proposed approach could also be applied with other sensors and land surface products (e.g., Duveiller et al. (2011)). Acquisitions from the future satellite Sentinel-2, which will provide high resolution optical images globally each 2 – 5 days, and will include shortwave infrared bands, will be of great help to progress in this field. In the future, a generalization of the approach described in this paper will include as well the validation of surface energy fluxes, at coarse resolution using estimates from higher spatial resolution sensors, accounting for the footprint of the sensor.

Acknowledgements

The Formosat-2 images used in this paper are ©NSPO (2006), distributed by SPOT Image S.A. All rights reserved. We are grateful to Prof. Crystal Schaaf (University of Massachusetts, Boston) for providing us with the MCD43D V006 data that are yet to be released, as well as for the valuable discussions with her and Dr. Qingsong Sun (Boston University). We would also like to thank the farmers for allowing us to make use of their fields for in situ measurements. We kindly thank the three anonymous reviewers for their valuable comments and suggestions that have significantly improved this article. This work was made through different projects funded by the Centre National d'Études Spatiales, CNES (TOSCA) and the European SIRRIMED (Sustainable use of irrigation water in the Mediterranean) FP7 project. Maria Mira was supported by a CNES postdoctoral contract, followed by a "Juan de la Cierva" postdoctoral contract from the Spanish Ministry of Economy and Competitiveness.

References

Baillarin, S., Gigord, P., & Hagolle, O. (2008). Automatic registration of optical images, a stake for future missions: Application to ortho-rectification, time series and mosaic products. In, *Proceedings of the IEEE International Geoscience and Remote Sensing Symposium* (pp. 1112-1115). Boston, MA, USA

Baillarin, S., Gleyzes, J.P., Latry, C., Vesco, C., Bouillon, A., Breton, E., Cunin, L., & Delvit, J.M. (2004). Validation of an automatic image ortho-rectification processing. In, *Proceedings of the IEEE International Geoscience and Remote Sensing Symposium, Vols 1-7: Science for Society: Exploring and Managing a Changing Planet* (pp. 1398-1401). New York, USA

Barnes, W.L., Pagano, T.S., & Salomonson, V.V. (1998). Prelaunch characteristics of the Moderate Resolution Imaging Spectroradiometer (MODIS) on EOS-AM1. *IEEE Transactions on Geoscience and Remote Sensing, 36*, 1088-1100

Bastiaanssen, W.G.M., Menenti, M., Feddes, R.A., & Holtslag, A.A.M. (1998). A remote sensing surface energy balance algorithm for land (SEBAL) - 1. Formulation. *Journal of Hydrology, 213*, 198-212

Bhattacharya, B.K., Mallick, K., Patel, N.K., & Parihar, J.S. (2010). Regional clear sky evapotranspiration over agricultural land using remote sensing data from Indian geostationary meteorological satellite. *Journal of Hydrology, 387*, 65-80

Brovkin, V., Boysen, L., Raddatz, T., Gayler, V., Loew, A., & Claussen, M. (2013). Evaluation of vegetation cover and land-surface albedo in MPI-ESM CMIP5 simulations. *Journal of Advances in Modeling Earth Systems, 5*, 48-57

Bsaibes, A., Courault, D., Baret, F., Weiss, M., Olioso, A., Jacob, F., Hagolle, O., Marloie, O., Bertrand, N., Desfond, V., & Kzemipour, F. (2009). Albedo and LAI estimates from FORMOSAT-2 data for crop monitoring. *Remote Sensing of Environment, 113*, 716-729

Cescatti, A., Marcolla, B., Vannan, S.K.S., Pan, J.Y., Roman, M.O., Yang, X.Y., Ciais, P., Cook, R.B., Law, B.E., Matteucci, G., Migliavacca, M., Moors, E., Richardson, A.D., Seufert, G., & Schaaf, C.B. (2012). Intercomparison of MODIS albedo retrievals and in situ measurements across the global FLUXNET network. *Remote Sensing of Environment, 121*, 323-334

Chern, J.S., & Wu, A.M. (2003). Some aspects of ROCSAT-2 system engineering. *Acta Astronautica, 54*, 145-151

Claverie, M., Vermote, E.F., Weiss, M., Baret, F., Hagolle, O., & Demarez, V. (2013). Validation of coarse spatial resolution LAI and FAPAR time series over cropland in southwest France. *Remote Sensing of Environment, 139*, 216-230

Courault, D., Bsaibes, A., Kpemlie, E., Hadria, R., Hagolle, O., Marloie, O., Hanocq, J.F., Olioso, A., Bertrand, N., & Desfonds, V. (2008). Assessing the potentialities of FORMOSAT-2 data for water and crop monitoring at small regional scale in South-Eastern France. *Sensors, 8*, 3460-3481

Cracknell, A.P. (1998). Synergy in remote sensing - what's in a pixel? *International Journal of Remote Sensing, 19*, 2025-2047

Davin, E.L., Seneviratne, S.I., Ciais, P., Olioso, A., & Wang, T. (2014). Preferential cooling of hot extremes from cropland albedo management. *Proceedings of the National Academy of Sciences of the United States of America, 111(27)*, 9757-9761

Duveiller, G., Baret, F., & Defourny, P. (2011). Crop specific green area index retrieval from MODIS data at regional scale by controlling pixel-target adequacy. *Remote Sensing of Environment, 115*, 2686-2701

Duveiller, G., & Defourny, P. (2010). A conceptual framework to define the spatial resolution requirements for agricultural monitoring using remote sensing. *Remote Sensing of Environment, 114*, 2637-2650

GCOS (2006). Systematic observation requirements for satellite-based products for climate. In, *Global Climate Observing System (GCOS)-107, WMO/TD No. 1338. World Meteorological Organization, Geneva, Switzerland*

Gomez-Chova, L., Zurita-Milla, R., Alonso, L., Amoros-Lopez, J., Guanter, L., & Camps-Valls, G. (2011). Gridding artifacts on medium-resolution satellite image time series: MERIS case study. *IEEE Transactions on Geoscience and Remote Sensing, 49*, 2601-2611

Hagolle, O., Dedieu, G., Mougenot, B., Debaecker, V., Duchemin, B., & Meygret, A. (2008). Correction of aerosol effects on multi-temporal images acquired with constant viewing angles: Application to Formosat-2 images. *Remote Sensing of Environment, 112*, 1689-1701

Hagolle, O., Huc, M., Villa Pascual, D., & Dedieu, G. (2015). A multi-temporal and multi-spectral method to estimate aerosol optical thickness over lands, for the atmospheric correction of FormoSat-2, LandSat, VENμS and Sentinel-2 images. *Remote Sensing (accepted)*

Holben, B.N., Eck, T.F., Slutsker, I., Tanre, D., Buis, J.P., Setzer, A., Vermote, E., Reagan, J.A., Kaufman, Y.J., Nakajima, T., Lavenu, F., Jankowiak, I., & Smirnov, A. (1998). AERONET - A federated instrument network and data archive for aerosol characterization. *Remote Sensing of Environment, 66*, 1-16

Huang, C.Q., Townshend, J.R.G., Liang, S.L., Kalluri, S.N.V., & DeFries, R.S. (2002). Impact of sensor's point spread function on land cover characterization: assessment and deconvolution. *Remote Sensing of Environment, 80*, 203-212

ISO (1992). Solar energy. Calibration of field pyranometers by comparison to a reference pyranometer. In, *International Organization for Standardization (ISO) 9847*

Jacob, F., Olioso, A., Gu, X.F., Su, Z.B., & Seguin, B. (2002a). Mapping surface fluxes using airborne visible, near infrared, thermal infrared remote sensing data and a spatialized surface energy balance model. *Agronomie, 22*, 669-680

Jacob, F., Olioso, A., Weiss, M., Baret, F., & Hautecoeur, O. (2002b). Mapping short-wave albedo of agricultural surfaces using airborne PolDER data. *Remote Sensing of Environment, 80*, 36-46

Jin, Y.F., Schaaf, C.B., Woodcock, C.E., Gao, F., Li, X.W., Strahler, A.H., Lucht, W., & Liang, S.L. (2003). Consistency of MODIS surface bidirectional reflectance distribution function and albedo retrievals: 2. Validation. *Journal of Geophysical Research-Atmospheres, 108*

Ju, J., Roy, D.P., Shuai, Y., & Schaaf, C. (2010). Development of an approach for generation of temporally complete daily nadir MODIS reflectance time series. *Remote Sensing of Environment, 114*, 1-20

Kimes, D.S., Sellers, P.J., & Newcomb, W.W. (1987). Hemispherical reflectance variations of vegetation canopies and implications for global and regional energy budget studies. *Journal of Climate and Applied Meteorology, 26*, 959-972

Lewis, P., & Barnsley, M.J. (1994). Influence of the sky radiance distribution on various formulations of the earth surface albedo. In, *Proceedings on the 6th International Symposium on Physical Measurements and Signatures in Remote Sensing* (pp. 707-715). Val d'Isere, France

Li, X.W., & Strahler, A.H. (1992). Geometric-optical bidirectional reflectance modeling of the discrete crown vegetation canopy : effect of crown shape and mutual shadowing. *IEEE Transactions on Geoscience and Remote Sensing, 30*, 276-292

Liang, S., Fang, H., Chen, M., Shuey, C.J., Walthall, C., Daughtry, C., Morisette, J., Schaaf, C., & Strahler, A. (2002). Validating MODIS land surface reflectance and albedo products: methods and preliminary results. *Remote Sensing of Environment, 83*, 149-162

Liang, S.L., Strahler, A.H., & Walthall, C. (1999). Retrieval of land surface albedo from satellite observations: A simulation study. *Journal of Applied Meteorology, 38*, 712-725

Liu, J., Schaaf, C., Strahler, A., Jiao, Z., Shuai, Y., Zhang, Q., Roman, M., Augustine, J.A., & Dutton, E.G. (2009). Validation of Moderate Resolution Imaging Spectroradiometer (MODIS) albedo retrieval algorithm: Dependence of albedo on solar zenith angle. *Journal of Geophysical Research-Atmospheres, 114*, 1-11

Lucht, W., Hyman, A.H., Strahler, A.H., Barnsley, M.J., Hobson, P., & Muller, J.P. (2000a). A comparison of satellite-derived spectral albedos to ground-based broadband albedo measurements modeled to satellite spatial scale for a semidesert landscape. *Remote Sensing of Environment, 74*, 85-98

Lucht, W., Schaaf, C.B., & Strahler, A.H. (2000b). An algorithm for the retrieval of albedo from space using semiempirical BRDF models. *IEEE Transactions on Geoscience and Remote Sensing, 38*, 977-998

Markham, B.L. (1985). The Landsat sensors' spatial responses. *IEEE Transactions on Geoscience and Remote Sensing, 23*, 864-875

Merlin, O. (2013). An original interpretation of the wet edge of the surface temperature-albedo space to estimate crop evapotranspiration (SEB-1S), and its validation over an irrigated area in northwestern Mexico. *Hydrology and Earth System Sciences, 17*, 3623-3637

Mira, M., Olioso, A., Gallego-Elvira, B., Courault, D., Garrigues, S., Marloie, O., Hagolle, O., Guillevic, P., & Boulet, G. (2015). Uncertainty assessment of surface net radiation derived from Landsat images. *Remote Sensing of Environment (undergoing review)*

Nishihama, M., Wolfe, R.E., Solomon, D., Patt, F.S., Blanchette, J., Fleig, A.J., & Masuoka, E. (1997). MODIS Level 1A Earth location: Algorithm theoretical basis document. NASA Technical Memorandum SDST-092. In. Greenbelt, MD: Goddard Space Flight Center SDST-092, Version 3.0

Olioso, A., Chauki, H., Courault, D., & Wigneron, J.P. (1999). Estimation of evapotranspiration and photosynthesis by assimilation of remote sensing data into SVAT models. *Remote Sensing of Environment, 68*, 341-356

Pinty, B., & Verstraete, M.M. (1992). On the design and validation of surface bidirectional reflectance and albedo models. *Remote Sensing of Environment, 41*, 155-167

Remer, L.A., Tanre, D., Kaufman, Y.J., Levy, R., & Mattoo, S. (2006). Algorithm for remote sensing of tropospheric aerosol from MODIS: Collection 5. Product ID: MOD04/MYD04. In, *MOD04 Algorithm Theoretical Basis Document* (p. 87 pp.)

Roman, M.O., Gatebe, C.K., Schaaf, C.B., Poudyal, R., Wang, Z., & King, M.D. (2011). Variability in surface BRDF at different spatial scales (30 m-500 m) over a mixed agricultural landscape as retrieved from airborne and satellite spectral measurements. *Remote Sensing of Environment, 115*, 2184-2203

Roman, M.O., Gatebe, C.K., Shuai, Y., Wang, Z., Gao, F., Masek, J.G., He, T., Liang, S., & Schaaf, C.B. (2013). Use of in situ and airborne multiangle data to assess MODIS and Landsat-based estimates of directional reflectance and albedo. *IEEE Transactions on Geoscience and Remote Sensing, 51*, 1393-1404

Roman, M.O., Schaaf, C.B., Lewis, P., Gao, F., Anderson, G.P., Privette, J.L., Strahler, A.H., Woodcock, C.E., & Barnsley, M. (2010). Assessing the coupling between surface albedo derived from MODIS and the fraction of diffuse skylight over spatially-characterized landscapes. *Remote Sensing of Environment, 114*, 738-760

Roman, M.O., Schaaf, C.B., Woodcock, C.E., Strahler, A.H., Yang, X., Braswell, R.H., Curtis, P.S., Davis, K.J., Dragoni, D., Goulden, M.L., Gu, L., Hollinger, D.Y., Kolb, T.E., Meyers, T.P., Munger, J.W., Privette, J.L., Richardson, A.D., Wilson, T.B., & Wofsy, S.C. (2009). The MODIS (Collection V005) BRDF/albedo product: Assessment of spatial representativeness over forested landscapes. *Remote Sensing of Environment, 113*, 2476-2498

Ross, J. (1981). The radiation regime and architecture of plant stands. The Hague, Netherlands: Junk Publishers

Salomon, J.G., Schaaf, C.B., Strahler, A.H., Gao, F., & Jin, Y.F. (2006). Validation of the MODIS Bidirectional Reflectance Distribution Function and albedo retrievals using combined observations from the Aqua and Terra platforms. *IEEE Transactions on Geoscience and Remote Sensing, 44*, 1555-1565

Schaaf, C., Shuai, Y., Wang, Z., Strahler, A.H., Zhang, X., Roy, D.P., Wolfe, R.E., Strabala, K., & Gumley, L. (2010). Monitoring albedo and vegetation phenology with the modis daily direct broadcast reflectance anisotropy algorithm. In, *American Geophysical Union* (p. 87 pp.). Washington, DC, USA, Tech. Rep. IN33C-03, 2010

Schaaf, C.B., Wang, Z., & Strahler, A.H. (2011). Commentary on Wang and Zender-MODIS snow albedo bias at high solar zenith angles relative to theory and to in situ observations in Greenland. *Remote Sensing of Environment, 115*, 1296-1300

Schaepman-Strub, G., Schaepman, M.E., Painter, T.H., Dangel, S., & Martonchik, J.V. (2006). Reflectance quantities in optical remote sensing-definitions and case studies. *Remote Sensing of Environment, 103*, 27-42

Schowengerdt, R.A. (2007). *Remote sensing: Models and methods for image processing*. (3 ed.). San Diego

Shuai, Y., Masek, J.G., Gao, F., Schaaf, C.B., & He, T. (2014). An approach for the long-term 30-m land surface snow-free albedo retrieval from historic Landsat surface reflectance and MODIS-based a priori anisotropy knowledge. *Remote Sensing of Environment, 152*, 467-479

Susaki, J., Yasuoka, Y., Kajiwara, K., Honda, Y., & Hara, K. (2007). Validation of MODIS albedo products of paddy fields in Japan. *IEEE Transactions on Geoscience and Remote Sensing, 45*, 206-217

Tan, B., Woodcock, C.E., Hu, J., Zhang, P., Ozdogan, M., Huang, D., Yang, W., Knyazikhin, Y., & Myneni, R.B. (2006). The impact of gridding artifacts on the local spatial properties of MODIS data: Implications for validation, compositing, and band-to-band registration across resolutions. *Remote Sensing of Environment, 105*, 98-114

Tang, R., Li, Z.-L., & Tang, B. (2010). An application of the Ts-VI triangle method with enhanced edges determination for evapotranspiration estimation from MODIS data in arid and semi-arid regions: Implementation and validation. *Remote Sensing of Environment, 114*, 540-551

Tanré, D., Deschamps, P.Y., Duhaut, P., & Herman, M. (1987). Adjacency effect produced by the atmophere scattering in Thematic Mapper data. *Journal of Geophysical Research, 92*, 12000-12006

Vermote, E.F., ElSaleous, N., Justice, C.O., Kaufman, Y.J., Privette, J.L., Remer, L., Roger, J.C., & Tanre, D. (1997). Atmospheric correction of visible to middle-infrared

EOS-MODIS data over land surfaces: Background, operational algorithm and validation. *Journal of Geophysical Research-Atmospheres, 102*, 17131-17141

Vermote, E.F., & Kotchenova, S. (2008). Atmospheric correction for the monitoring of land surfaces. *Journal of Geophysical Research-Atmospheres, 113*

Wang, Z., Schaaf, C.B., Chopping, M.J., Strahler, A.H., Wang, J., Roman, M.O., Rocha, A.V., Woodcock, C.E., & Shuai, Y. (2012). Evaluation of Moderate-resolution Imaging Spectroradiometer (MODIS) snow albedo product (MCD43A) over tundra. *Remote Sensing of Environment, 117*, 264-280

Wang, Z., Schaaf, C.B., Strahler, A.H., Chopping, M.J., Roman, M.O., Shuai, Y., Woodcock, C.E., Hollinger, D.Y., & Fitzjarrald, D.R. (2014). Evaluation of MODIS albedo product (MCD43A) over grassland, agriculture and forest surface types during dormant and snow-covered periods. *Remote Sensing of Environment, 140*, 60-77

Weiss, M., Baret, F., Garrigues, S., & Lacaze, R. (2007). LAI and fAPAR CYCLOPES global products derived from VEGETATION. Part 2: validation and comparison with MODIS collection 4 products. *Remote Sensing of Environment, 110*, 317-331

Weiss, M., Baret, F., Leroy, M., Begue, A., Hautecoeur, O., & Santer, R. (1999). Hemispherical reflectance and albedo estimates from the accumulation of across-track sun-synchronous satellite data. *Journal of Geophysical Research-Atmospheres, 104*, 22221-22232

Weiss, M., Demarty, J., Baret, F., Peylin, P., & Prunet, P. (2009). Processing the remote sensing medium spatial resolution (MERIS) and high sptial resolution (SPOT). In, *CAMELIA: Technical report on satellite data (WP215, 216 & 217)* (p. 72)

WMO (2008). Guide to meteorological instruments and methods of observation, Chapter 7: Measurement of radiation. In, *World Meteorological Organization (WMO)-No.8*. Geneve, Switzerland. ISBN 978-92-63-10008-5

Wolfe, R.E., Nishihama, M., Fleig, A.J., Kuyper, J.A., Roy, D.P., Storey, J.C., & Patt, F.S. (2002). Achieving sub-pixel geolocation accuracy in support of MODIS land science. *Remote Sensing of Environment, 83*, 31-49

Wolfe, R.E., Roy, D.P., & Vermote, E. (1998). MODIS land data storage, gridding, and compositing methodology: Level 2 grid. *IEEE Transactions on Geoscience and Remote Sensing, 36*, 1324-1338

WWW1 Validation status for BRDF/Albedo (MCD43). *http://landval.gsfc.nasa.gov/ProductStatus.php?ProductID=MOD43 [last access: June 19, 2014]*

WWW2 Level 1 and Atmosphere Archive and Distribution System (LAADS). *http://laadsweb.nascom.nasa.gov/ [last access: June 19, 2014]*

WWW3 Actual (blue-sky) albedo computation. *http://www.umb.edu/spectralmass/terra_aqua_modis/modis_user_tools [last access: June 19, 2014]*

WWW4 MODIS Reprojection Tool *https://lpdaac.usgs.gov/tools/modis_reprojection_tool [last access: June 19, 2014]*

FIGURES

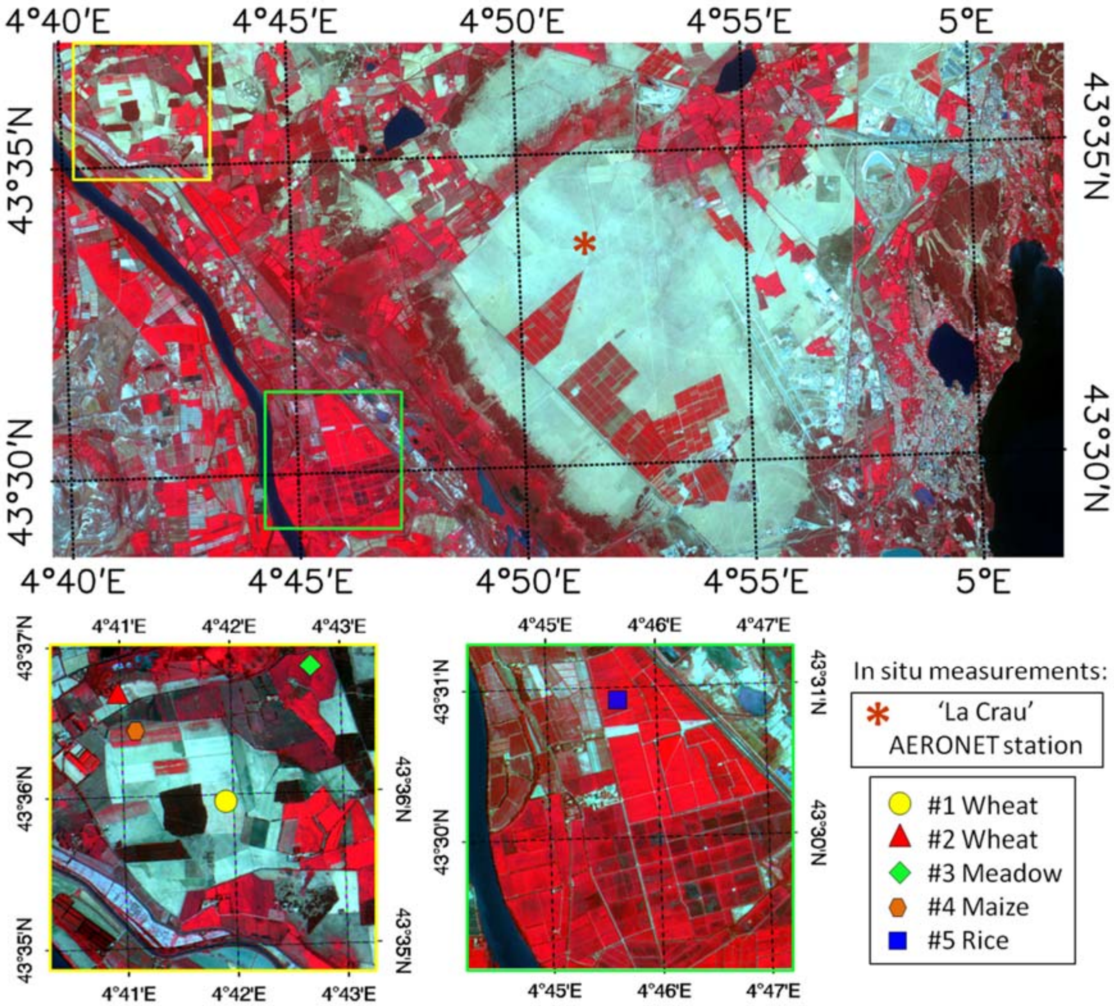

Fig. 1. Color composite (bands 4-3-2) of the cropped Formosat-2 image (8-m spatial resolution) acquired on July 23rd, 2006 over the Crau-Camargue area, South-Eastern France. The AERONET station over 'La Crau' is indicated in the upper image, and fields where in situ measurements of albedo were performed are represented in the lower frames. Exceptionally, #5 rice field does not correspond to the location of field measurements, since they were made outside the Formosat-2 scanned region, but to the location of pixels considered for the comparison. #1 and #2 wheat fields turned to bare soils at the end of June.

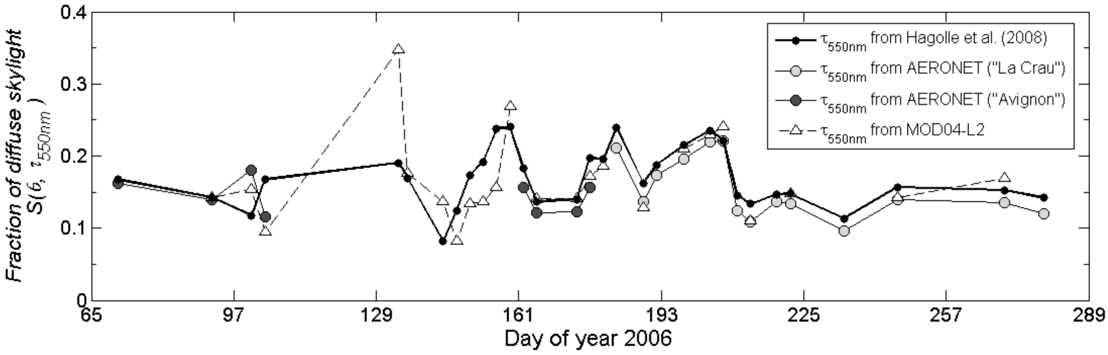

Fig. 2. Temporal variation of fraction of diffuse skylight as estimated by the different sources for aerosol optical depth (τ).

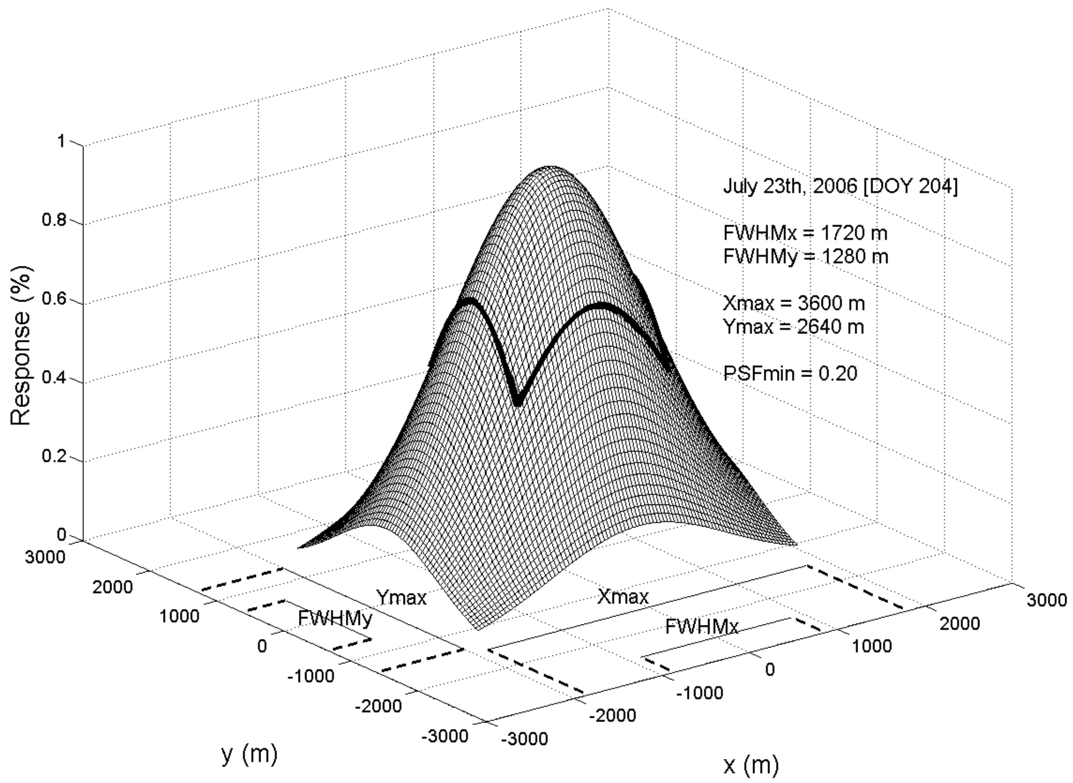

Fig. 3. Equivalent point spread function of MCD43D albedo at 1 km over the Crau-Camargue site (July 23rd, 2006). Distances are calculated in meters from the center of the observation footprint. In bold, limit of the function defined by the $FWHM_x$ and $FWHM_y$.

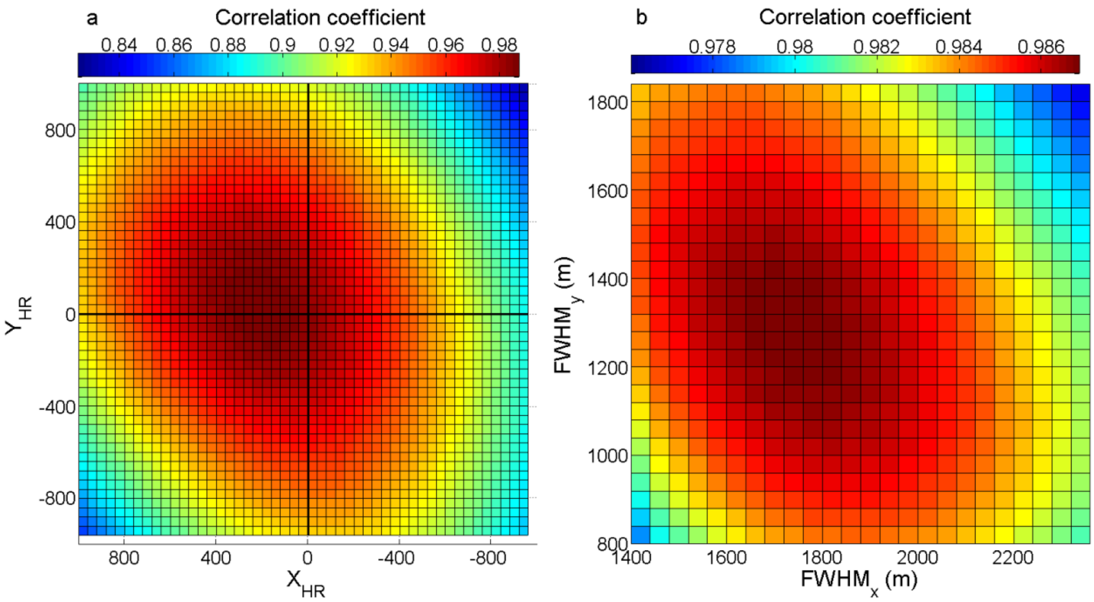

Fig. 4. Correlation coefficient between MODIS blue-sky albedo and Formosat-2 albedo convolved with the PSF for images acquired on July 23rd, 2006 for **(a)** each shift of the Formosat-2 image (indicated by X_{HR} and Y_{HR}) for the optimized PSF size, and **(b)** each PSF size (given by $FWHM_x$ and $FWHM_y$) for the optimized X_{HR} and Y_{HR}.

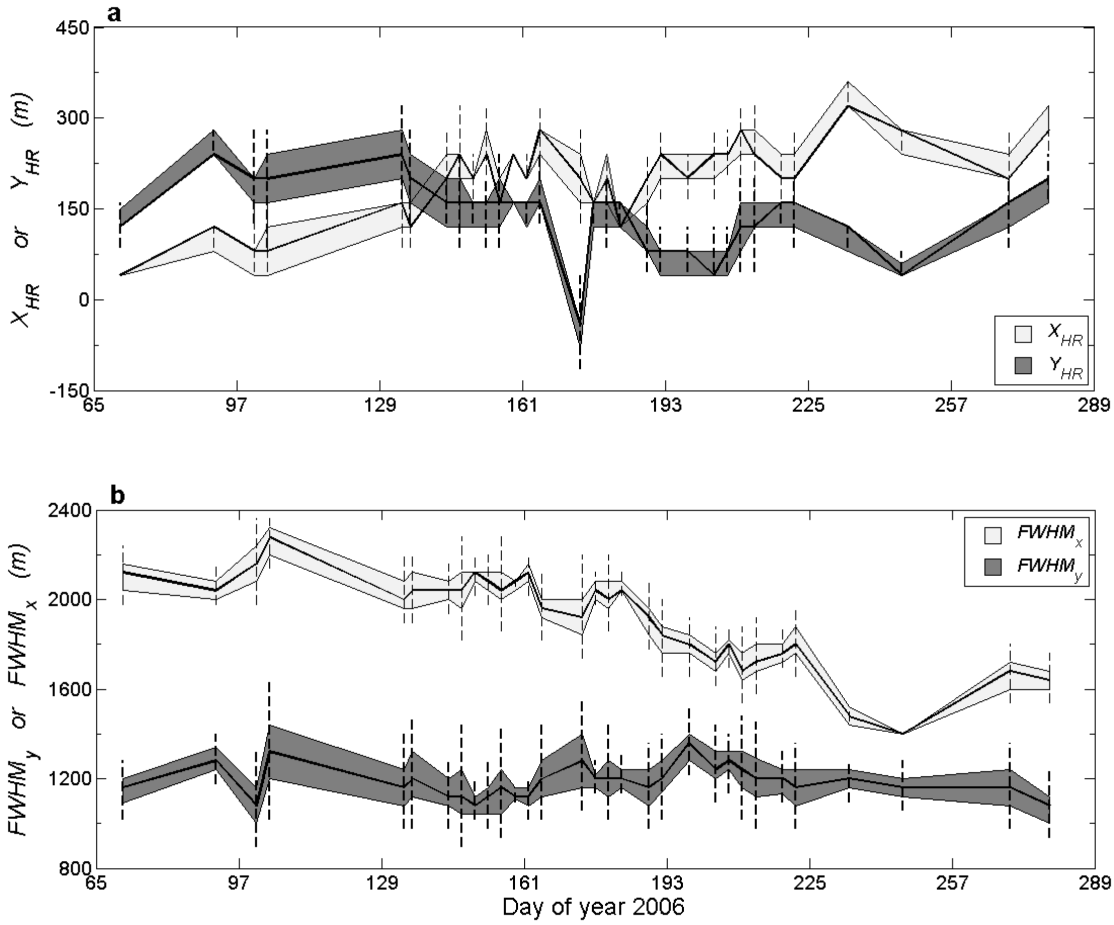

Fig. 5. Results from the comparison of MODIS blue-sky albedo and Formosat-2 albedo convolved with the PSF, by changing the PSF size (in $FWHM_x$ and $FWHM_y$) and the shifting of the Formosat-2 image (up to 1000 m in both directions, indicated by X_{HR} and Y_{HR}) in steps of 40 m. Boxplots for **(a)** shifts and **(b)** PSF sizes, giving the maximum correlation coefficient within ±0.001 precision, for the optimized PSF sizes and shifts, respectively. Each boxplot belongs to an acquisition day and comprises the median (i.e., crossed by a continuous line), the first and third quartile (i.e., comprised by the shaded areas), and the extreme values excluding outliers (i.e., inferior and superior whiskers).

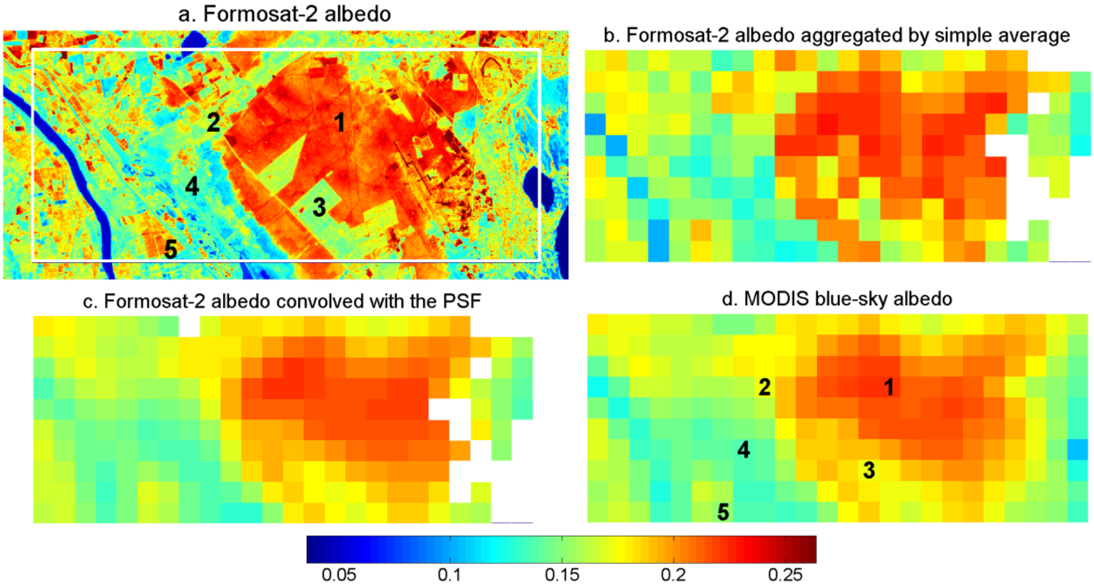

Fig. 6. Images of albedo over the Crau-Camargue, South Eastern France, on July 23rd, 2006. The area within the white inner rectangle in **(a)** corresponds to the area plotted in **(b)**, **(c)** and **(d)**, while the outer pixels are included within the PSF ($FWHM_x$=1720 m; $FWHM_y$=1280m; PSF_{min}=0.20). For this scanned area, any pixel was masked by the quality flag of MODIS. Selected pixels in **(d)** (and corresponding location in **(a)**) labeled with numbers correspond to quite homogeneous areas in land cover, specified in Table 2.

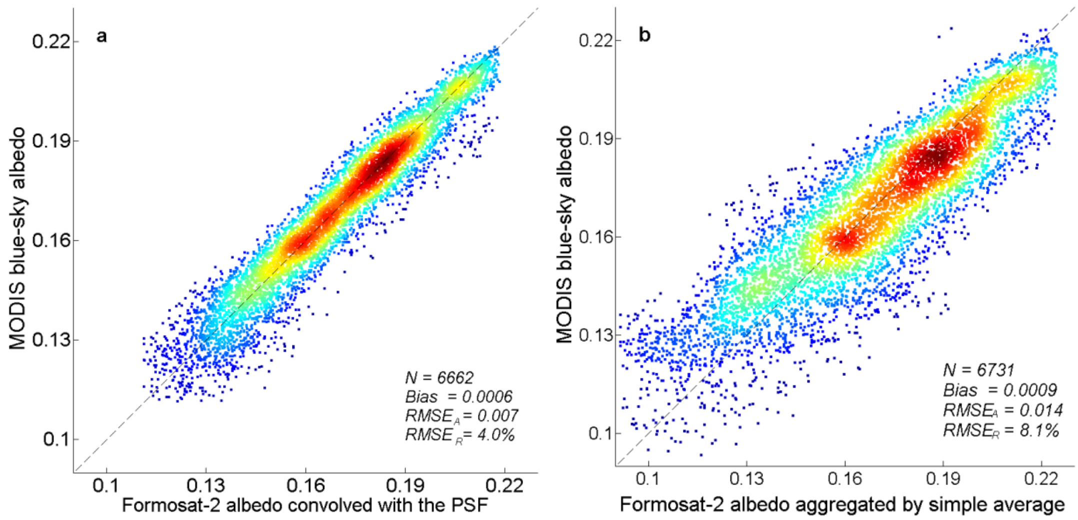

Fig. 7. Density scatter plots between MODIS blue-sky albedo and Formosat-2 albedo convolved with the PSF **(a)** or aggregated by simple average **(b)**, using data from the 31 images from 2006. Reddish points indicate high density. There were excluded pixels masked by the quality flag of MODIS, pixels including more than 50% area classified as cloud, cloud's shadow, water or urban land cover, and outliers (i.e., out the 0.5% and 99.5% percentiles). *N*: number of samples used for the comparison; $RMSE_A$ and $RMSE_R$: absolute and relative Root Mean Square Error, respectively.

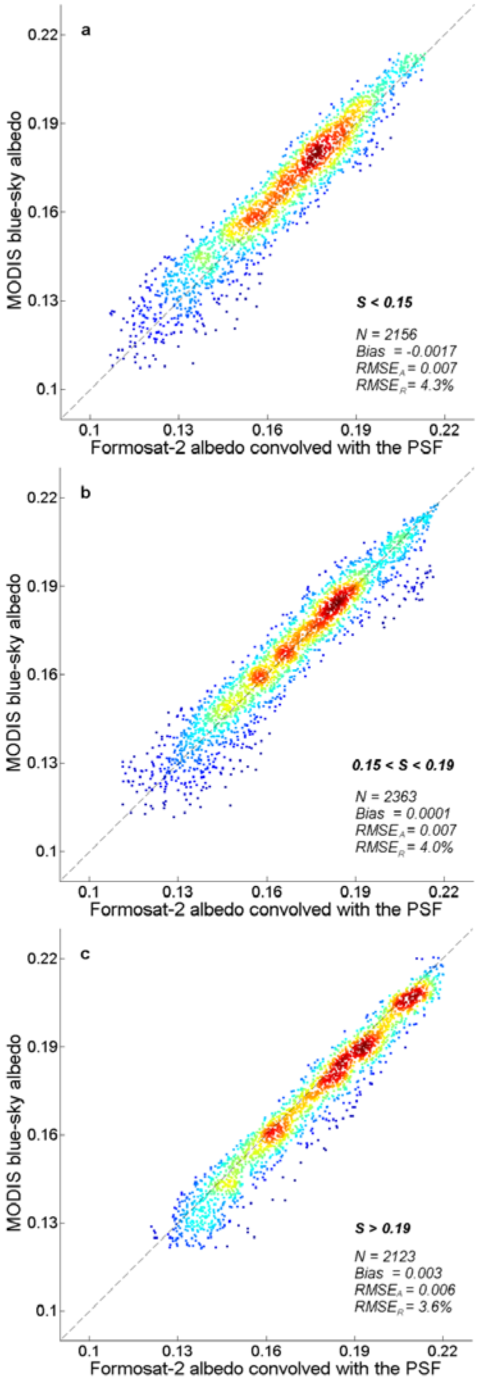

Fig. 8. Density scatter plots between MODIS blue-sky albedo and Formosat-2 albedo convolved with the PSF using data from days with certain values for the fraction of diffuse skylight (*S*). There were excluded pixels masked by the quality flag of MODIS, pixels including more than 50% area classified as cloud, cloud's shadow, water or urban land cover, and outliers (i.e., out the 0.5% and 99.5% percentiles). *N*: number of samples used for the comparison; $RMSE_A$ and $RMSE_R$: absolute and relative Root Mean Square Error, respectively.

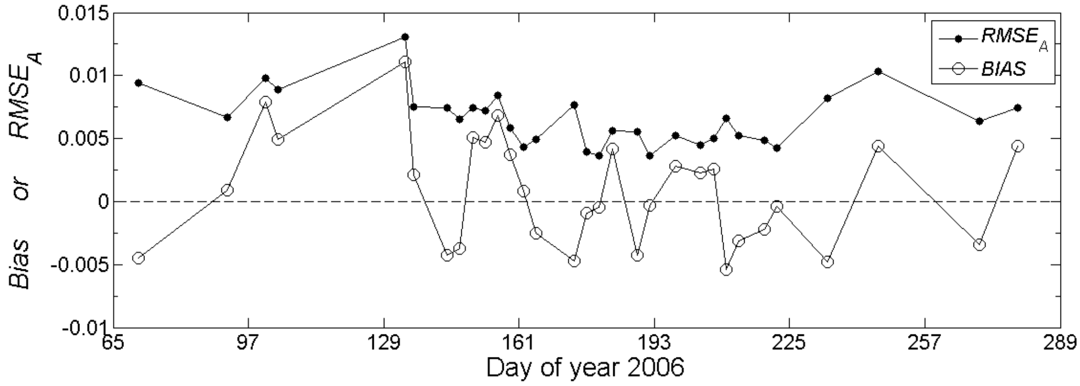

Fig. 9. Statistical metrics from evaluation of MODIS blue-sky albedo with Formosat-2 albedo convolved with the PSF. $RMSE_A$: absolute Root Mean Square Error.

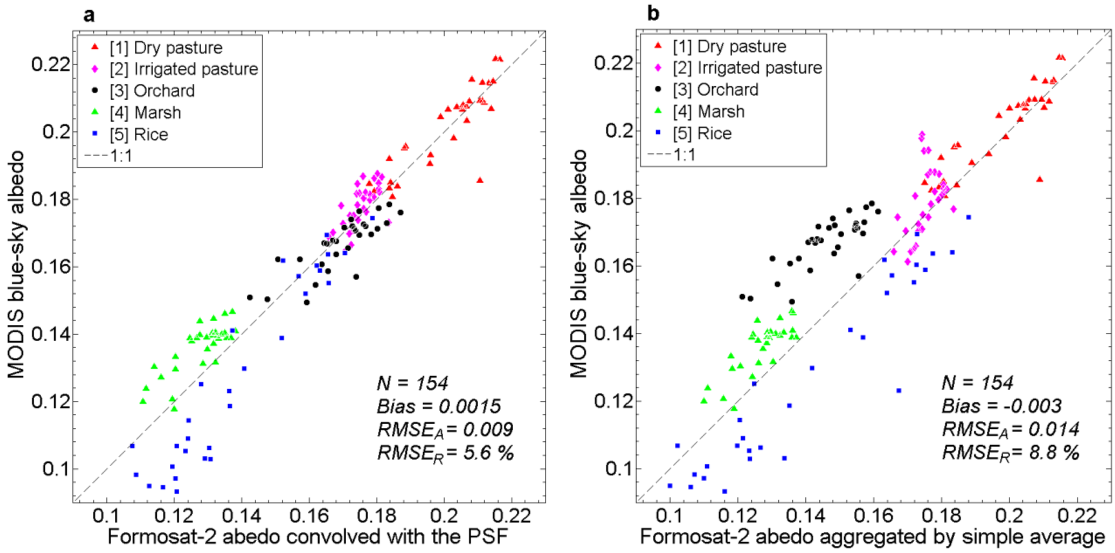

Fig. 10. Evaluation of MODIS blue-sky albedo with Formosat-2 albedo convolved with the PSF **(a)** or aggregated by simple average **(b)** over several 1-km pixels with a predominant land cover type, specified in Table 2 and located in Fig. 6d. *N*: number of samples used for the comparison; $RMSE_A$ and $RMSE_R$: absolute and relative Root Mean Square Error, respectively.

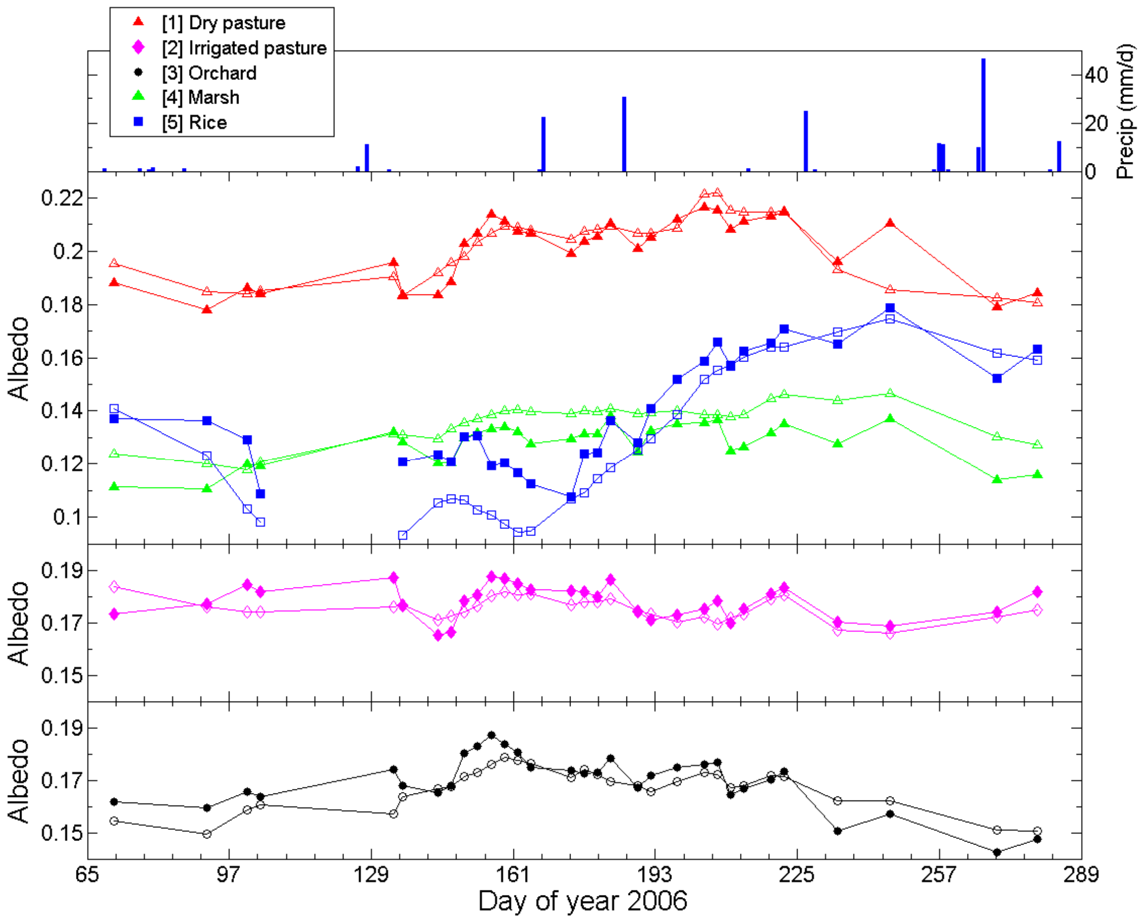

Fig. 11. Rainfall events (top) and albedo dynamics from MODIS (non-filled symbols) and Formosat-2 convolved with the PSF (filled symbols) over five selected 1-km pixels, with characteristics specified in Table 2 and location in Fig. 6d.

TABLES

Table 1. MODIS BRDF/albedo product MCD43: specifications and science data sets provided. All products are global, Level 3 and have been assigned a “Validated (Stage 3) Status”. MCD43D product only available from Collection V006. MCD meaning combined product of Terra and Aqua acquisitions; *fiso*, *fvol*, *fgeo*: weighting parameters associated with the *RossThickLiSparseReciprocal* BRDF model; broad bands: 0.3-0.7 µm, 0.7-5.0 µm, and 0.3-5.0 µm.

Collection	**Temporal resolution**		
V005	8-days (with 16 days of acquisition)		
V006	Daily (with 16 days of acquisition)		
Product name	**Spatial resolution**	**Projection**	
MCD43**A***	500 m	Sinusoidal	
MCD43**B***	1 km	Sinusoidal	
MCD43**C***	0.05 Deg CMG	Lat/Lon	
MCD43**D***	30 arcsec	Lat/Lon	
Product type	**Product name**	**Science data sets provided in V005 and V006**	**Science data sets only provided in V006**
BRDF/albedo model parameters	MCD43**A1/B1/C1** and MCD43**D01-30**	*fiso*, *fvol*, *fgeo* for each MODIS band and three broad bands	-
BRDF/albedo quality	MCD43**A2/B2/C2** and MCD43**D31-D41**	Albedo quality, local solar noon, valid observations, and snow status for each MODIS band and three broad bands	Uncertainty for each MODIS band and three broad bands
Albedo	MCD43**A3/B3/C3** and MCD43**D42-51/D52-61**	White-sky and black-sky albedo (at local solar noon) for each MODIS band and three broad bands	Albedo mandatory quality for each MODIS band and three broad bands
Nadir BRDF-adjusted reflectances (NBAR)	MCD43**A4/B4/C4** and MCD43**D62-68**	NBAR product (at local solar noon) for each MODIS band	Albedo mandatory quality for each MODIS band and three broad bands

1

Table 2. Main land cover types within each selected 1-km pixel (location specified in Fig. 6d), and performances from the evaluation of MODIS blue-sky albedo by considering data from the 31 dates. $RMSE_A$ and $RMSE_R$: absolute and relative Root Mean Square Error, respectively.

	Land cover	**Accuracy (bias)**	**Uncertainty ($RMSE_A$)**	**Relative uncertainty ($RMSE_R$, %)**
[1]	100 % dry pastures	0.000	0.006	3.1%
[2]	80 % irrigated pastures 14 % industrial irrigated orchards 6 % urban	0.003	0.005	3.0%
[3]	100 % industrial irrigated orchards	0.003	0.006	3.8%
[4]	89 % marshes 11 % industrial irrigated orchards	-0.008	0.009	7.3%
[5]	90 % rice 9 % urban	0.011	0.015	10.7%